Editors' Suggestion

Magnetic anisotropy, magnetoelastic coupling, and the magnetic phase diagram of $Ni_{0.25}Mn_{0.75}TiO_3$

A. Elghandour,[1,*] L. Gries,[1] L. Singer,[1] M. Hoffmann,[1] S. Spachmann,[1] M. Uhlarz,[2] K. Dey,[1,†] and R. Klingeler[1,‡]

[1]*Kirchhoff Institute for Physics, Heidelberg University, INF 227, 69120 Heidelberg, Germany*

[2]*Dresden High Magnetic Field Laboratory (HLD-EMFL), Helmholtz-Zentrum Dresden-Rossendorf, 01328 Dresden, Germany*

(Received 3 March 2023; accepted 1 June 2023; published 5 July 2023)

Thermodynamic and magnetic studies on high-quality single crystals are used to investigate the magnetic phase diagram and magnetostructural coupling in the mixed-spin system $Ni_{0.25}Mn_{0.75}TiO_3$. Clear anomalies in the thermal expansion at the spin ordering and spin reorientation temperatures, T_N and T_R, evidence pronounced magnetoelastic effects. The magnetic entropy is released mainly above T_N implying considerable short range magnetic order up to about $4 \times T_N$. This is associated with a large regime of negative thermal expansion of the c axis. Both T_N and T_R exhibit the same sign of uniaxial pressure dependence, which is positive (negative) for pressure applied along the b (c) axis. The magnetic phase diagrams are constructed and the uniaxial pressure dependencies of the ordering phenomena are determined. For magnetic fields $B \parallel b$ axis, a sign change and splitting of anomalies implies further magnetic phases. In addition to short-range magnetic order well above T_N, competing anisotropies yield a glasslike behavior as evidenced by a maximum in AC-χ ($T_{SG} \simeq 3.7$ K) and quasilinear temperature dependence of c_p. High-field magnetization up to 50 T demonstrates that in addition to antiferromagnetically ordered spins there are also only weakly coupled moments at 2 K with a sizable amount of about 15% of all Mn^{2+} spins present in the material. The observed changes in the pressure dependence and the magnetostrictive effects shed light on the recently observed flop of electric polarization from $P \parallel c$ to $P \parallel a$ [Phys. Rev. B **90**, 144429 (2014)], in particular, suggesting that the magnetoelectric effect is not directly related to magnetostriction.

DOI: 10.1103/PhysRevB.108.014406

I. INTRODUCTION

Mixed antiferromagnetic (AFM) systems with competing magnetic anisotropies have been extensively studied with regard to their underlying physics and as a platform to realize spin-glass states [1–5]. In such mixed AFM systems where, e.g., a magnetic ion (M) is partly substituted by another one (N), i.e., forming $M_{1-x}N_x$, long-range magnetic order appears in the vicinity of $x = 0$ and $x = 1$, whereas, it is suppressed at intermediate doping levels. The spin arrangement in the AFM long-range-ordered state is basically that of the parent compounds but with two different AFM sublattices resulting from the induced modulation around the magnetic ions [6,7] and the difference in their ionic radii [8,9]. A typical example is mixed ilmenite-structured titanates, $A_xMn_{1-x}TiO_3$ (A = Fe, Co, and Ni), where the substituent A is randomly distributed in the structure. Although, at intermediate x, spin-glass-like phases are observed, AFM long-range order evolves near the end sides of the phase diagrams and is suppressed in the doped systems [10–18]. The parent compounds $ATiO_3$ (A = Mn, Fe, Co, Ni) crystallize in a hexagonal lattice with space-group $R\bar{3}$ [19]. $MnTiO_3$ exhibits G-type AFM order with the crystallographic direction c as the magnetically easy axis [20]. In contrast, $FeTiO_3$, $NiTiO_3$, and $CoTiO_3$ show A-type AFM order with an easy-plane-like anisotropy perpendicular to the c axis [20–23]. This implies not only different exchange interactions, but also competing anisotropies in the mixed systems $A_xMn_{1-x}TiO_3$.

Experimental studies on $Ni_xMn_{1-x}TiO_3$ started three decades ago by Ito *et al.* [13] and Yoshizawa *et al.* [14] to address theoretical predictions [1,6] on the mixed AFM compounds and revived after the discovery of linear magnetoelectric effect (ME) in $MnTiO_3$ [24]. The general trends in $Ni_xMn_{1-x}TiO_3$ upon increasing the Ni-content x are as the following [13,15]: Initially, G-type AFM order is suppressed, and a spin-reoriented phase appears around $x \sim 0.2$. Specifically, at $x = 0.33$, G-type AFM order evolves at $T_N = 27.6$ K and spin reorientation at $T_R = 17.5$ K. The latter is accompanied by a flop in the electric polarization [18]. At intermediate concentrations, $0.38 \leqslant x \leqslant 0.45$, a spin-glass phase emerges [15–17,25]. Within this glassy phase and particularly at $x = 0.42$, $Ni_xMn_{1-x}TiO_3$ exhibits a linear ME [15,16]. Further increasing the Ni content to $x \geqslant 0.48$ results in an A-type AFM long-range-ordered phase, which does not show ME [18].

Here, we report detailed thermodynamic and magnetic studies on $Ni_{0.25}Mn_{0.75}TiO_3$ single crystals grown by the optical floating-zone technique. Our dilatometric studies provide quantitative information on magnetoelastic coupling in the mixed AFM system. These investigations have been motivated by recent studies on the parent compounds $MnTiO_3$ and $NiTiO_3$, which display pronounced thermal expansion

*ahmed.elghandour@kip.uni-heidelberg.de

†Present address: Clarendon Laboratory, University of Oxford, Parks Road, Oxford, OX1 3PU, United Kingdom.

‡klingeler@kip.uni-heidelberg.de

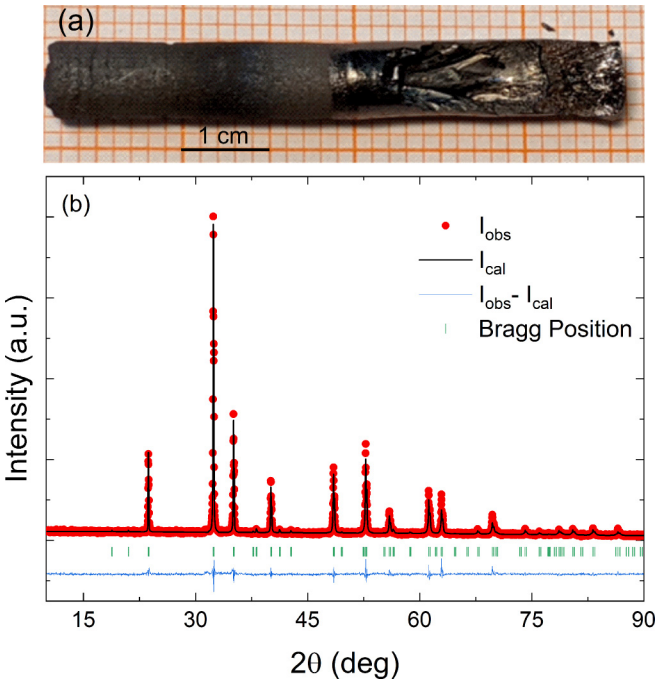

FIG. 1. (a) Picture of the $Ni_{0.25}Mn_{0.75}TiO_3$ boule grown under a 5-bar argon atmosphere. (b) Rietveld refinement fit (black line) of the room temperature XRD pattern (red markers) of a powdered $Ni_{0.25}Mn_{0.75}TiO_3$ single crystal. The difference between the observed and the calculated pattern is shown in blue. Vertical ticks in green denote the allowed Bragg positions of the ilmenite phase.

and magnetostriction anomalies associated with magnetic ordering and spin reorientation [26–28]. The present thermodynamic data elucidate magnetoelastic coupling in the *G*-type AFM-ordered phase and in the spin reoriented phase of $Ni_{0.25}Mn_{0.75}TiO_3$. Sharp anomalies in the thermal expansion and magnetostriction coefficients enable us to construct the magnetic phase diagrams and to identify an additional magnetic phase, thereby illustrating the interplay of spin and structure in the mixed anisotropic system under study. We also find that short-range correlations persist up to about $4 \times T_N$.

II. SINGLE-CRYSTAL GROWTH AND EXPERIMENTAL METHODS

Macroscopic single-crystals of $Ni_{0.25}Mn_{0.75}TiO_3$ were grown by the floating-zone technique in a high-pressure optical furnace [29,30] (HKZ, Scidre). Figure 1(a) shows a representative $Ni_{0.25}Mn_{0.75}TiO_3$ boule grown in Ar atmosphere at 5-bar pressure (Ar flow of 0.3 l/min) and at a growth rate of 12 mm/h with counterrotating rods at 10–25 rpm. The employed polycrystalline feed rods were made from stoichiometric amounts of NiO, MnO_2, and TiO_2 precursors similar to the procedure described in Ref. [26]. The single-crystal growth parameters were optimized in a series of growth experiments at various Ar:O_2 atmosphere mixtures, pressures, growth rates, and rotation speeds [31]. The phase purity of the grown crystals was confirmed by powder XRD (pXRD) studies of pulverized single crystals using a Bruker D8 Advance ECO diffractometer with Cu $K\alpha$ radiation [Fig. 1(b)]. The simulation of the pXRD data was performed

TABLE I. Fractional atomic coordinates, Wyckhoff positions, and site occupation of $Ni_{0.25}Mn_{0.75}TiO_3$ as obtained from the refinement of powder XRD measurements at 300 K. The overall factor is set as $B_{ov} = 2.278\ 55$ and the isotropic Debye-Waller factor B_{iso} is fixed to zero. [Space-group: *R*-3 (148), $a = b = 5.113\,259$ Å, $c = 14.147\,032$ Å ($\chi^2 = 2.82$), $\alpha = \beta = 90°$, $\gamma = 120°$.]

Atom	Site	*x*	*y*	*z*	Occ
Ni	6*c*	0	0	0.35474	0.07999
Mn	6*c*	0	0	0.35474	0.25333
Ti	6*c*	0	0	0.14201	0.33333
O	18*f*	0.33329	0.04030	0.23906	1.00000

by means of Rietveld refinements using the FULLPROF suite 2.0 [32] [see Fig. 1(b) and Table I). The composition was investigated by energy dispersive x-ray spectroscopy (EDX) using a JEOL JSM-7610F scanning electron microscope with a Thermo Scientific UltraDry silicon drift x-ray detector. The analysis yields a Ni:Mn ratio of 0.235(5):0.765(5), whereas, the ratio (Ni+Mn):Ti agrees to 1 within the error bars. Finally, from the grown boule, millimeter-sized grains were obtained, oriented for measurements along the [010], [$2\bar{1}0$], and [001] crystallographic axes and cut to cuboids. Their crystallinity was confirmed by Laue diffraction in backscattering geometry. The crystal structure was studied by means of single-crystal XRD at 100 K with Mo $K\alpha$ radiation ($\lambda = 0.71073$ Å) using an Agilent Technologies Supernova-E CCD four-circle diffractometer. The structural refinements confirm the $R\bar{3}$ space group and improve the accuracy of the crystallographic parameters. The obtained lattice parameters and relevant crystallographic information are listed in Table II.

The obtained lattice parameters are in between the values for the parent compounds $MnTiO_3$ ($a = 5.133\,93(6)$ Å, $c = 14.268\,79(15)$ Å [31]) and $NiTiO_3$ ($a = 5.0304$ Å, $c = 13.7862$ Å [26]) and are slightly larger than the values found for $x = 0.33$ (5.12 and 14.15 Å) [18]. The reduced unit-cell volume upon increasing the Ni^{2+} concentration can be attributed to negative chemical pressure due to the different ionic radii of Mn^{2+} (0.83 Å) and Ni^{2+} (0.69 Å) [33]. By means of the lattice parameters of the end members, Vegard's law can be used to further confirm the doping level of $x \simeq 0.25$.

TABLE II. Selected crystallographic parameters from the EDX studies and from refinement of single-crystal XRD data obtained at 100 K.

Composition from EDX (Ni:Mn)	0.235(5):0.765(5)
Molar mass	151.69 g/mol
Crystal system, space group	Trigonal, $R\bar{3}$ (no. 148)
Unit cell:	
a	5.10799(4) Å
c	14.12863(11) Å
Calculated density	4.739 g/cm^3
Reflections collinear/independent	14886/1066 ($R_{int} = 0.023$)
Goodness-of-fit on F^2	1.172

The magnetization was studied by means of the Magnetic Properties Measurement System (superconducting quantum interference device, Quantum Design) and the Physical Properties Measurement System (PPMS-vibrating-sample magnetometer, Quantum Design) on an oriented single crystal of $Ni_{0.25}Mn_{0.75}TiO_3$ in the temperature range of 2 to 300 K and in magnetic fields up to 7 and 14 T, respectively. At low applied magnetic fields, both field-cooled (FC) and zero-field-cooled (ZFC) protocols were applied where the sample was cooled either in the external measurement field or the field was applied after cooling to the lowest temperature. The AC magnetization was measured in the temperature range from 2 to 40 K with 9-Oe AC excitation field, up to 3-T DC magnetic fields and frequencies ranging from 2 to 10 kHz, using the ACSMII option of the PPMS. Pulsed-magnetic-field magnetization was measured up to 50 T at Helmholtz Zentrum Dresden-Rossendorf by an induction method using a coaxial pick-up coil system [34]. The pulse raising time was 7 ms. The pulsed-field magnetization data were calibrated using static magnetic-field magnetization data obtained by means of PPMS. The specific-heat capacity was measured in the temperature range of 1.8–300 K using the heat-capacity option of the PPMS. High-resolution dilatometry measurements were performed by means of a three-terminal high-resolution capacitance dilatometer in a home-built setup placed inside a Variable Temperature Insert of an Oxford magnet system [35,36]. With this dilatometer, the relative length changes dL_i/L_i along the crystallographic b and c directions, respectively, were measured on an oriented cuboid-shaped single crystal of dimensions $2.400(2) \times 2.128(2) \times 0.559(2)\,\mathrm{mm}^3$. Measurements were performed in the temperature range of 2–300 K and in magnetic fields up to 15 T, applied along the direction of the measured length changes. The linear thermal expansion coefficients $\alpha_i = 1/L_i dL_i(T)/dT$ were obtained. In addition, the field-induced length changes, $dL_i(B_i)$, were measured at different fixed temperatures between 2 and 40 K and in magnetic fields up to 15 T. The longitudinal magnetostriction coefficients, $\lambda_i = 1/L_i dL_i(B_i)/dB_i$, were derived.

III. EVOLUTION OF MAGNETIC ORDER AT $B = 0$ T

In zero magnetic field, $Ni_{0.25}Mn_{0.75}TiO_3$ exhibits two magnetic phase transitions as evidenced by the static magnetic susceptibility and the specific heat in Fig. 2. Specifically, there is a jumplike feature in the specific-heat c_p/T at $T_N = 34.8(6)$ K and a rather symmetric hump at $T_R \sim 14.8(4)$ K [see Fig. 2(c)]. The jump at T_N amounts to $\Delta c_p \approx 0.54(11)$ J/(mol K). The magnetic nature of both transitions is evident from associated anomalies in the static magnetic susceptibility and its derivative as shown in Figs. 2(a) and 2(b), respectively. At high temperatures, the magnetic susceptibility χ_i along the different crystallographic axes i obey a Curie-Weiss-like behavior (see Fig. 1 in the Supplemental Material (SM) [37]). At T_N, χ_c displays a clear kink whereas only very small anomalies are observed for the other directions, thereby confirming the easy magnetic c axis in the long-range -ordered phase below T_N. This is particularly evident when Fisher's specific-heat $\partial(\chi T)/\partial T$ is considered, which is proportional to the magnetic specific heat [38]. It displays a λ-shaped behavior only for the $B \parallel c$ axis [Fig. 2(b)]. Upon further cooling, the

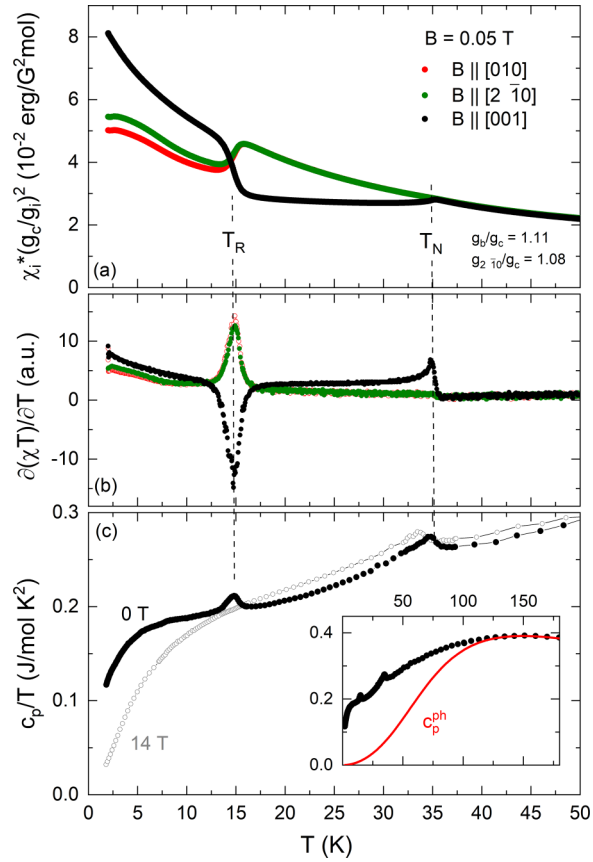

FIG. 2. (a) Static magnetic susceptibility $\chi = M/B$, of $Ni_{0.25}Mn_{0.75}TiO_3$ as a function of temperature measured along three different crystallographic directions at applied magnetic-field $B = 0.05$ T. The data have been normalized to the c-axis g factor as fitted to the high-temperature behavior. (b) Corresponding derivatives $\partial(\chi T)/\partial T$. (c) Specific-heat capacity, represented by c_p/T, measured both at zero magnetic field and at $B \parallel = 14$ T. The inset shows the zero-field specific-heat data over an extended temperature range, including an estimated representation of the phononic background (see the text). The vertical dashed lines mark the onset of the long-range magnetic ordering at T_N and the spin reorientation at T_R.

jumplike features, visible in the magnetic susceptibility χ_i at T_R, suggest rotation of the spins into the ab plane. We note the discontinuous nature of the anomaly at T_R.

Fitting χ_c between 175 and 300 K by means of an extended Curie-Weiss law including a temperature-independent term, χ_0, yields the Curie constant $C = 3.5(2)$ erg K mol^{-1} G^2, the Weiss temperature $\Theta = -112(6)$ K, and $\chi_0 = 8.05 \times 10^{-4}$ erg mol^{-1} G^{-2}. Differences in the static magnetic susceptibilities χ_i at high temperatures can be explained by the ratio g_{010}:$g_{2\bar{1}0}$:$g_{001} \simeq$ 2:1.94:1.8 of the corresponding g factors (g_i) (see Fig. 2 in the SM). The large negative value of the Weiss temperature indicates the presence of dominant antiferromagnetic exchange interactions, aligning with the previously recorded neutron-scattering results on $Ni_{0.33}Mn_{0.67}TiO_3$ [18]. The effective moment $\mu_{\mathrm{eff}} \approx 5.2(1)\mu_B$ is derived from the Curie constant. It agrees well with the expected value calculated using the g-factors g_{Mn} and g_{Ni} of the parent compounds [26,39].

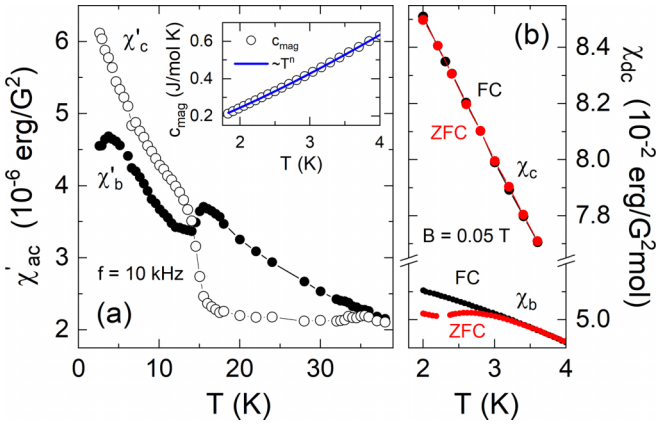

FIG. 3. (a) Real part of AC magnetic susceptibility of $Ni_{0.25}Mn_{0.75}TiO_3$ measured along the crystallographic b and c axes at $f = 10$ kHz. The inset: Magnetic specific heat at low temperatures. The (blue) line represents a fit to the data (see the text). (b) Static magnetic susceptibility measured along the crystallographic b and c axes at $B = 0.05$ T, highlighting the differences between FC and ZFC measurements.

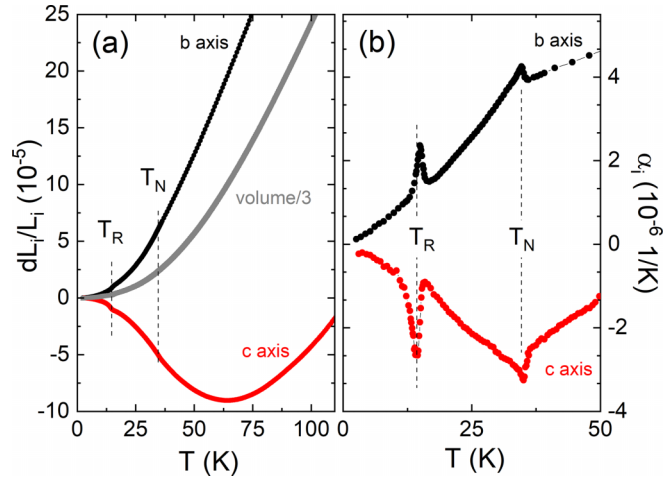

FIG. 4. (a) Relative length changes dL_i/L_i ($i = b$ and c), of $Ni_{0.25}Mn_{0.75}TiO_3$ measured along the crystallographic i axis in zero applied magnetic field; light gray markers represent the relative volume changes. (b) Corresponding uniaxial thermal expansion coefficients α_i. The dashed lines mark T_N and T_R.

AC magnetic susceptibility studies confirm the anomalies at T_N and T_R, but do not indicate any frequency dependence in the regime of $2.5 \leqslant f \leqslant 10$ kHz (see Fig. 3 in the SM). We also do not observe any finite dissipative signal χ''. In χ_b', apart from the anomalies observed at T_N and T_R, we observe an additional broad maximum at $T^* \approx 3.7$ K as depicted in Fig. 3(a) T^* corresponds to the beginning of a thermal hysteresis region seen in χ_b between the ZFC and the FC data as shown in Fig. 3(b). In contrast, no thermal hysteresis is observed in χ_c and χ_c'. In the same temperature regime, the magnetic specific heat shows no anomaly but follows a $c_p(T) \propto T^n$ behavior with $n \approx 1.3(1)$ [see the inset of Fig. 3(a)]. We note that the observed exponent n does not correspond to the expectations $c_p(T) \propto T^3$ describing the low-temperature magnon excitations in a long-range-ordered three-dimensional (3D) antiferromagnet [40].

The onset of long-range magnetic order at T_N and spin reorientation at T_R are associated with distinct lattice changes as demonstrated by clear anomalies in the thermal expansion (see Fig. 4). In addition, the thermal expansion exhibits an anisotropic behavior up to the highest measured temperatures. The evolution of magnetic order is signaled by kinks in the relative length changes dL_i/L_i at T_N and by slightly λ-shaped anomalies in its corresponding thermal expansion coefficients α_i. Although there is a positive thermal expansion of the b axis in the whole temperature regime under study, the c axis initially shrinks upon heating and expands only above $T = 60$ K. Opposite trends for the different axes are also observed for the actual anomalies in α_i at T_N, which show opposite signs. Qualitatively, the anomalies in α_i imply a positive uniaxial pressure dependence ($\partial T_{N/R}/\partial p_b > 0$) of T_N and T_R, whereas, both are suppressed by uniaxial pressure applied along the c axis.

A. Magnetic phase diagram

Applying magnetic fields up to 15 T hardly changes the long-range-ordering temperature T_N but significantly affects the spin-reoriented phase and the associated transition temperature T_R. This is clearly visible in the specific-heat data shown in Fig. 2(c). At $B = 14$ T, whereas, the anomaly at T_R is completely suppressed, the one at T_N is only very slightly shifted to lower temperatures. Due to pronounced magnetoelastic coupling in $Ni_{0.25}Mn_{0.75}TiO_3$, which is evidenced in Fig. 4, the magnetic-field effects on the phase boundaries can be very well traced by thermal expansion and magnetostriction measurements. As displayed in Fig. 5, applying a field of $B = 1$ T yields a significant decrease (increase) of T_R when applied along the b axis (c axis). Notably, for the $B \parallel b$ axis, the anomaly at T_R changes its sign from positive to negative for $B \geqslant 1$ and up to $B = 14$ T [see Fig. 5(a)]. At low magnetic fields, the phase transition is also detected in the static magnetic susceptibility χ_b, which displays a noticeable jumplike feature at T_R and a corresponding peak in $\partial(\chi T)/\partial T$. However, these anomalies become weaker as the

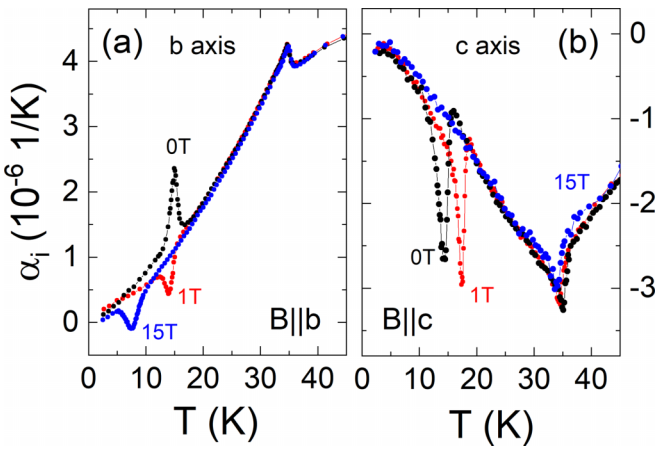

FIG. 5. Temperature dependence of the thermal expansion coefficient α_i ($i = b$ and c), measured at different applied magnetic fields along (a) the b axis, and (b) the c axis.

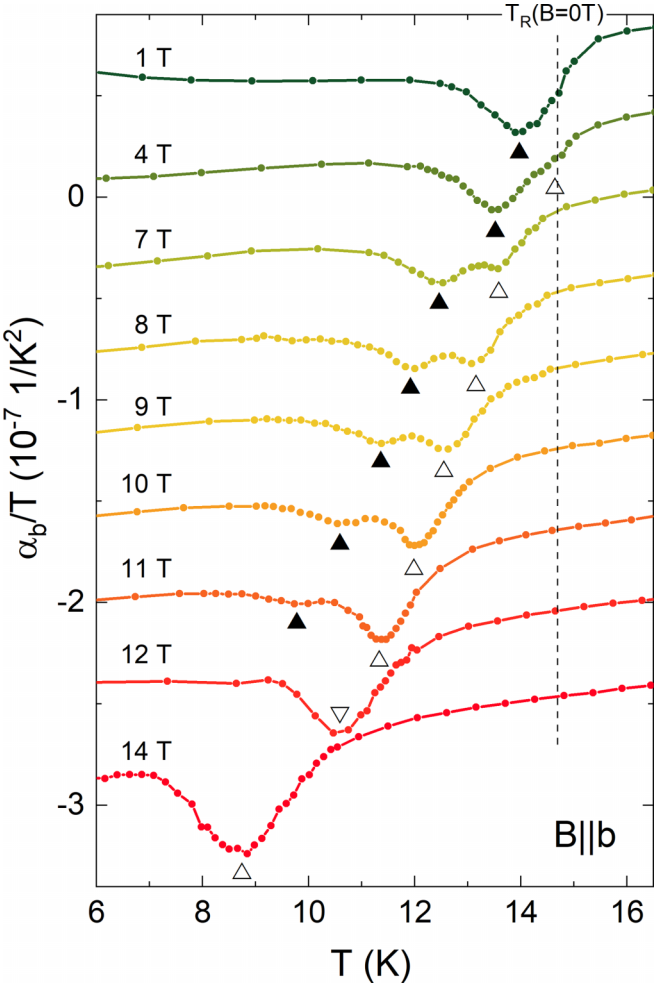

FIG. 6. Thermal expansion coefficient α_b/T at different magnetic fields $B \parallel b$ axis. Triangles mark two features as discussed in the text; the dashed line displays $T_R(B = 0\ \mathrm{T})$.

magnetic field gradually increases and completely vanish at magnetic-fields $B \parallel b \geqslant 0.8$ T (see Fig. 4 in the SM). The data, hence, imply that the sign change in α_b at T_R is accompanied by the disappearance of the anomalies observed in χ_b.

The evolution of the anomaly observed at T_R in α_b, $B \parallel b \geqslant 1$ T, is shown in Fig. 6. After the anomaly changed sign as evidenced by the data obtained at $B = 1$ T, an additional feature appears, which is only faint at 1 T but increases for larger fields, yielding two clearly separated features split by more than 1 K at 7 T. Both the emerged (marked by filled triangles) and the initial (marked by open triangles) features shift to lower temperatures with increasing the applied magnetic field, which indicates their antiferromagnetic nature. In addition, the emerged feature becomes more pronounced for higher fields, whereas, the initial one decreases until it is not detectable anymore above 11 T (see Fig. 6). In contrast, the thermal expansion and magnetization data signal a significant shift of T_R to higher temperatures when applying the $B||c$ axis so that the phase boundary merges into T_N slightly above 2 T (see Fig. 9, and Figs. 5 and 9 in the SM).

The G-type AFM phase appearing at zero magnetic field in the temperature regime $T_R < T < T_N$ (i.e., AF1 in Fig. 9)

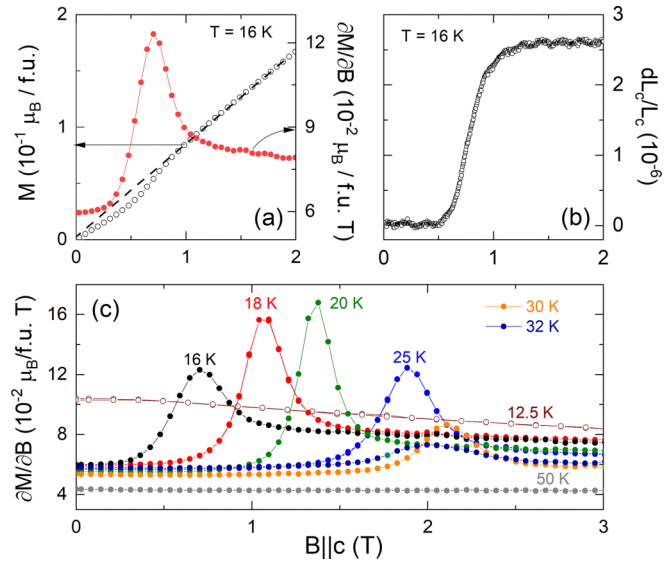

FIG. 7. (a) Isothermal magnetization, measured at 16 K, for the $B \parallel c$ axis and corresponding magnetic susceptibility $\partial M/\partial B$. The dashed line linearly extrapolates the high-field behavior to zero field. (b) Magnetostriction dL_c/L_c, at $T = 16$ K as a function of the magnetic-field $B \parallel c$ axis. (c) Magnetic susceptibility for the $B \parallel c$ axis in the temperature regime of 16 K $\leqslant T \leqslant$ 50 K. Peaks are associated with the spin-flip transition at B_{c2}.

is further investigated by magnetization and magnetostriction studies presented in Fig. 7. At $T = 16$ K, when the spins are predominately parallel to the c axis [18], magnetic fields $\parallel c$ yield a spin-flop-like transition at $B_{\mathrm{SF}} = 0.62(8)$ T [see Fig. 7(a)]. The critical field B_{SF} associated with this transition into the spin-reoriented phase (AF2 in Fig. 9) is signaled by the peaks in $\partial M/\partial B$. Upon heating, it shifts towards higher

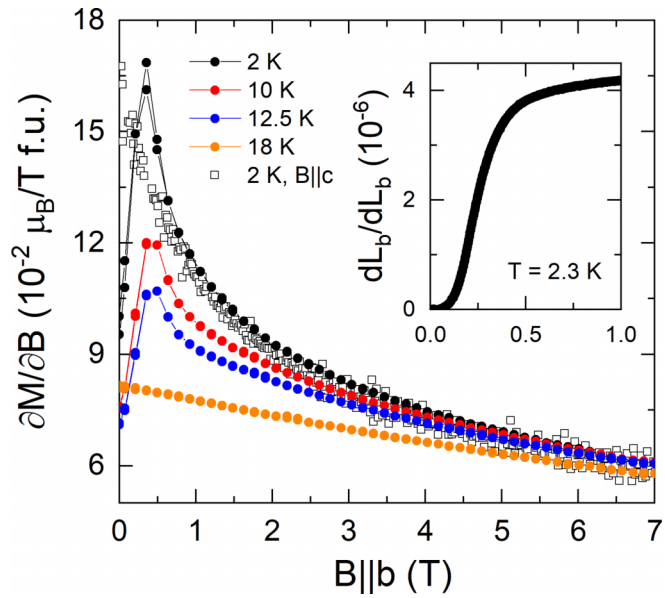

FIG. 8. Magnetic susceptibility $\partial M/\partial B$ in the temperature regime of 2 K $\leqslant T \leqslant$ 18 K for $B \parallel b$ axis. The peaks signal B_{c1} (see the text). Open squares show $\partial M/\partial B$ at 2 K with the $B \parallel c$ axis. The inset: Magnetostriction $dL_b/L_b(B \parallel b)$ at $T = 2.3$ K.

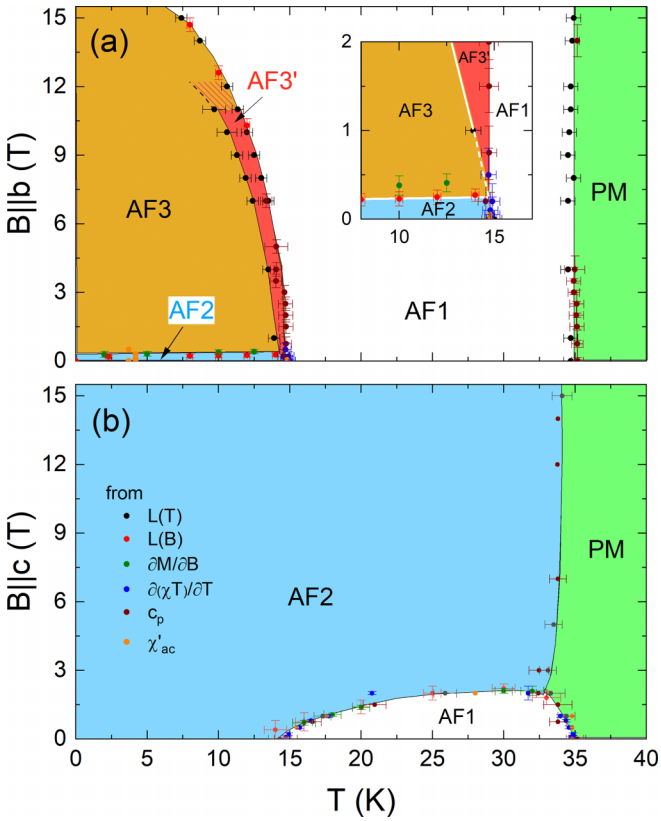

FIG. 9. Magnetic phase diagram of $Ni_{0.25}Mn_{0.75}TiO_3$ derived from magnetization $M(T, B)$, thermal expansion, and magnetostriction $L(T, B)$, χ_{ac}, and specific-heat data for the (a) $B \parallel b$ and (b) $B \parallel c$ axes. The insert in (a) shows the enlarged region around 15 K. The colors distinguish paramagnetic (PM), G-type AF (AF1), spin-reoriented AF (AF2), and field-induced AF phases (AF3/AF3′). T_N, T_R, B_{SF}, and B_{c1} are the associated phase boundaries described in the text.

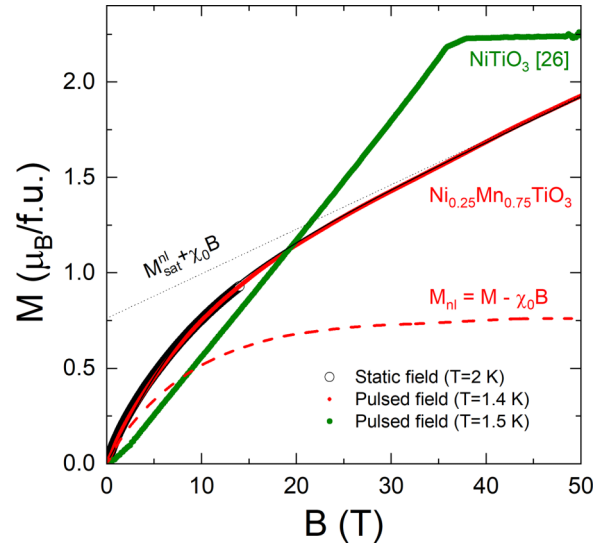

FIG. 10. Magnetization of $NiTiO_3$ (from Ref. [26]) and $Ni_{0.25}Mn_{0.75}TiO_3$ up to 50 T. Open circles show the averaged static field magnetization of $Ni_{0.25}Mn_{0.75}TiO_3$ single crystals measured up to 14 T. Pulsed-field data are from up sweeps. The data of $Ni_{0.25}Mn_{0.75}TiO_3$ are well described by the sum of a modified Brillouin function and a linear term $\chi_0 B$ (see the text). The dashed line shows the nonlinear magnetization $M_{nl} = M - \chi_0 B$.

fields and disappears above T_N [see Fig. 7(c)]. The metamagnetic transition is also characterized by a sharp increase of the c axis length amounting to $\Delta L_c/L_c = 2.6 \times 10^{-6}$ [Fig. 7(b)]. Below T_R, $B \| c$ does not drive a spin-flop transition [Fig. 7(c)], which agrees to the suggested spin rotation. In contrast, for $B \| b$ a metamagnetic transition appears only below T_R at a critical field of $B_{C1} \sim 0.4$ T, which barely depends on the temperature (Fig. 8). The high-field phase for $B \parallel b$ is labeled AF3 in Fig. 9). Again, the metamagnetic transition is associated with anomalous length changes (Fig. 8, the inset), amounting to $\Delta L_b/L_b = 3.9 \times 10^{-6}$ at $T = 2.3$ K.

The observed clear features in magnetization, thermal expansion, magnetostriction, and specific heat enable us to construct the magnetic phase diagrams for both $B \| b$ and $B \| c$ as shown in Fig. 9. For $B \| c$, the G-type antiferromagnetic phase with spins $\| c$ evolving in zero field at T_N (AF1 phase) forms a distinct dome bounded by $T_R(B)$ and $B_{SF}(T)$ towards the spin-reoriented AF2 phase [see Fig. 9(b)]. The transition AF1 to AF2 is associated with significant lattice changes. In the field region of the dome, T_N is visibly suppressed by $B \parallel c$, but it increases for higher fields ($B \parallel c > 2\,T$), which implies the relevance of critical fluctuations around the tricritical point. A field-driven magneto-structural transition is also observed for $B \| b$ where the low-field AF2 phase is separated by a rather field-independent phase boundary $B_{c1}(T)$ from the AF3 phase. Note, AF2 and AF3 phases feature uniaxial pressure dependencies of opposite sign. In contrast to T_N, which only very weakly depends on $B \parallel b$, AF3 is considerably suppressed and we extrapolate the upper critical field $B_c^{AF3} \simeq 17(2)$ T. Notably, starting from B_{c1}, an intermediate phase AF3′ appears. The thermal-expansion anomaly size associated with the phase boundary between AF3 and AF3′ continuously decreases when increasing $B \parallel b$ and cannot be detected above 11 T in our dilatometric data. This behavior suggests the decrease in the pressure dependence or negligible associated specific-heat changes. Since the boundary AF3/AF3′ is not associated with a clear anomaly in the magnetization, we neither can trace it by magnetic measurements in this regime of the phase diagram.

Lastly, our data reveal the presence of weakly coupled magnetic moments at low temperatures. In contrast to $NiTiO_3$ which magnetization increases linearly up to the saturation field as expected for an long-range-ordered AFM [26], magnetization of $Ni_{0.25}Mn_{0.75}TiO_3$ exhibits pronounced right-bending behavior (see Fig. 10). Note, that the pulsed-field powder magnetization data perfectly agree with the single-crystal studies up to 14 T. The data can be described by the sum of a modified Brillouin function B_S and a linear term, i.e., $M_{sat}B_S(x) + \chi_0 B$; $x = g\mu_B SB/[k_B(T + \Theta^*)]$ with M_{sat} as the saturation magnetization of the right-bending term, spin S, field-independent susceptibility χ_0, Boltzmann constant k_B, Bohr magneton μ_B, and the g factor. Θ^* is a parameter to account for magnetic interactions between the weakly coupled moments. The linear term mainly reflects the response of the long-ranged AF-ordered phase. The nonlinear term $M_{nl}(B) = M(B) - \chi_0 B$ implies the presence of rather weakly

coupled spins saturating already at intermediate fields. $M_{\rm sat}$ is the fully saturated moment of the weakly coupled spins. Phenomenologically, using $g = 1.99$ and $S = 5/2$ of the Mn^{2+} spins, the data are described by $\Theta^* = 15.5$ K, $M_{\rm sat} = 0.75$ μ_B/f.u., and $\chi_0 = 0.023$ μ_B/(T f.u.). The value of $M_{\rm sat}$ may be read from the data without fitting, and it clearly exceeds the fully saturated moment of all Ni^{2+} spins in $Ni_{0.25}Mn_{0.75}TiO_3$ ($S = 1$, $g = 2.14$, $M_{\rm sat}^{\rm Ni} \simeq 0.53$ μ_B/f.u.) [41] so that $M_{\rm nl}(B)$ cannot be attributed only to the Ni^{2+} subsystem. Attributing $M_{\rm nl}(B)$ to only Mn^{2+} spins would imply that about 15% of them are only weakly coupled. As will be pointed out below, this value might further increase at higher temperatures. In general, the observation of weakly coupled moments is in accordance with the observed low-temperature behavior of the static magnetic susceptibility displayed in Fig. 2(a) where for $B \parallel c$ a Curie-like increase is observed in the AFM-ordered phase. Concomitantly, both $\chi_{[010]}$ and $\chi_{[2\bar{1}0]}$ increase upon cooling below T_N, too, which behavior differs from what is expected in conventional antiferromagnets as it shows much larger magnetization with respect to the paramagnetic phase.

IV. DISCUSSION

Our data imply the evolution of long-range antiferromagnetic order at $T_N \simeq 35$ K and reorientation of the spin direction at $T_R \simeq 15$ K. This agrees to the sequence of phase transitions reported in the established phase diagram of $Ni_xMn_{1-x}TiO_3$ [13,15]. As compared to the mother compound $MnTiO_3$, which shows $T_N \simeq 64$ K, the tendency for long-range magnetic order is significantly reduced by Ni doping. Although our results fit the expected phase boundary $T_N(x)$, we find T_R in between the two temperatures proposed as the start and the end temperatures of the spin rotation in Ref. [13]. The onset of long-range magnetic order in $Ni_{0.25}Mn_{0.75}TiO_3$ at T_N is signaled by clear anomalies in $\chi_{B\parallel c}$, c_p, and thermal expansion (Figs. 2 and 4), which confirms the easy magnetic c axis and, in particular, shows significant magnetoelastic coupling. The negative thermal expansion along the c axis as well as strong magnetic-field effects on the specific heat well above T_N suggest the presence of short-range-ordering phenomena in the paramagnetic phase. The presence of short-range magnetic correlations above T_N results in associated magnetic entropy changes, which can be estimated by comparison with the bare lattice contribution. The latter may be obtained by fitting the specific heat well above T_N by an appropriate phononic model. This results in very similar phonon specific heat as found in $MnTiO_3$. Since, in the following, we will compare the entropy changes in $Ni_{0.25}Mn_{0.75}TiO_3$ and $MnTiO_3$, for the following entropy analysis, we employ the phonon specific heat from Ref. [28] and account for the different atomic masses by multiplying with 1.015 [see Fig. 11(a)].

Subtracting the lattice contribution from the measured specific heat gives the magnetic specific heat $c_p^{\rm mag}$. Integrating $c_p^{\rm mag}/T$ yields the magnetic entropy changes $\Delta S_{\rm m} = 12.3(7)$ J/(mol K), which is close to the full expected magnetic entropy of $0.75R \ln 6 + 0.25R \ln 3 \approx 13.4$ J/(mol K). Notably, our analysis implies magnetic entropy changes up to about 130 K, i.e., persistence of short-range magnetic order up to about $\simeq 4T_N$. The presence of considerable short-range magnetic order is further confirmed by the fact that the

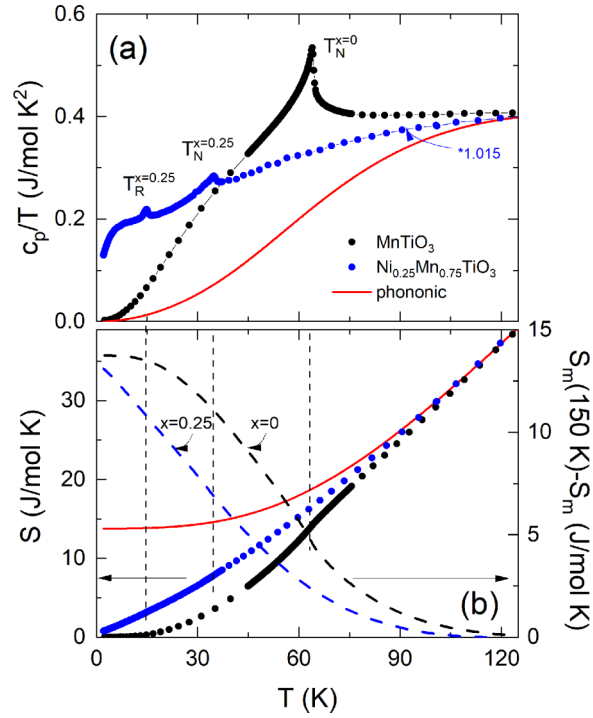

FIG. 11. (a) Temperature dependence of the specific-heat c_p/T of $Ni_xMn_{1-x}TiO_3$ with $x = 0$, i.e., $MnTiO_3$ (from Ref. [28]), and $x = 0.25$ measured at $B = 0$ T. The $Ni_{0.25}Mn_{0.75}TiO_3$ data are multiplied by 1.015 to account for the atomic mass difference. The red line presents the lattice contribution $c_p^{\rm ph}$ of $MnTiO_3$. (b) Corresponding entropy changes (left ordinate) derived from integrating c_p/T. $S_{\rm ph}(T)$ (red line) and $S_{x=0.25}(T)$ (blue circles) are shifted to match $S_{x=0}(T)$ above 120 K (see the text). Right ordinate: Changes in the magnetic entropy for both doping levels with respect to its value at 150 K.

observed anomaly Δc_p, at T_N, is rather small as it only amounts to a few percent of the value predicted by mean-field theory. Quantitatively, the specific-heat jump at T_N amounts to $\Delta c_p = 0.54(11)$ J/(mol K), which is only a very small fraction ($\approx$3%) of the expected mean-field value $\Delta c_p = R\frac{5S(S+1)}{S^2+(S+1)^2} \approx 18.9$ J/(mol K) [42]. Note, that the actual jump size associated with the measured anomaly can be even smaller as it may be superimposed by critical fluctuations. Such a small specific-heat anomaly implies significant short-range spin order above T_N and/or considerable spin disorder below T_N.

Our experimental data show short-range magnetic order well above T_N as well as weakly coupled moments and a glasslike behavior at low temperatures. In Fig. 11(b), we illustrate how magnetic entropy is consumed upon cooling by comparing the specific heat and entropy changes appearing in $Ni_{0.25}Mn_{0.75}TiO_3$ and $MnTiO_3$ [28] alongside the lattice contributions. In $MnTiO_3$, the specific-heat data illustrate a typical example of evolution of 3D long-range magnetic order. In $Ni_{0.25}Mn_{0.75}TiO_3$, at high temperatures, the specific-heat data are similar to those of $MnTiO_3$, which we attribute to the lattice. The main effects of 25% Ni doping are as follows: (1) Suppression of T_N and of the anomaly size as discussed above. (2) Upon cooling below T_N, in $Ni_{0.25}Mn_{0.75}TiO_3$, the entropy is consumed in a quasilinear manner, which qualitatively

differs from the behavior in $MnTiO_3$. This is particularly visible in Fig. 11(b), where in addition to the measured total entropy changes, the relative changes in the magnetic entropy with respect to the value at high temperature are shown. The figure illustrates how different magnetic order evolves in $Ni_{0.25}Mn_{0.75}TiO_3$ as compared to $MnTiO_3$. (3) In $Ni_{0.25}Mn_{0.75}TiO_3$, the low-temperature behavior exhibits a quasilinear behavior for $T \lesssim 4$ K where we find $c_p \sim T^{1.3}$ as shown in the inset of Fig. 3(a). This contrasts a T^3 behavior expected for a 3D AFM, which is observed in $MnTiO_3$. Quasilinear behavior of c_p at low temperatures was previously reported for the spin-glass state of $Ni_{0.42}Mn_{0.58}TiO_3$ [15] and for canonical spin-glass systems, such as CuMn [43] and ScGd [44].

The presence of considerable magnetic disorder evidenced by our analysis of the entropy changes qualitatively agrees with the observation of weakly coupled magnetic moments and a glassylike feature in the AC magnetic susceptibility ($T_{SG} \simeq 3.7$ K). For $Ni_{0.4}Mn_{0.6}TiO_3$, Solanki *et al.* observe a similar feature at 9.1 K and report an XY-like spin-glass state with quasi-two-dimensional antiferromagnetic order [17]. By inelastic neutron scattering studies, they conclude the presence of short-range-ordered antiferromagnetic clusters with short-lived spin correlations in the XY-like SG state. The latter observation may be associated with the presence of weakly antiferromagnetically coupled moments in $Ni_{0.25}Mn_{0.75}TiO_3$ as demonstrated by in the high-field magnetization data in Fig. 10. Our findings also raise the question of the origin of the glasslike behavior. One may speculate about a dynamic process, which involves partial freezing of weakly coupled moments at low temperatures resulting in the (at 1.4 K) experimentally observed number of weakly coupled moments. This scenario implies that the number of weakly coupled moments increases upon heating. However, our M vs B data do not enable us to distinguish the response of weakly coupled moments from the entire magnetic response at higher temperatures. The observed number of about 15% of all Mn^{2+} spins present in the material at 1.4 K may, hence, increase at higher temperatures.

Magnetoelastic coupling is further analyzed by quantifying and comparing the thermal expansion and the heat-capacity anomalies in α_i and c_p. The ratio of these quantities yields the uniaxial and hydrostatic pressure dependencies of the associated ordering phenomena by exploiting the Clausius-Clapeyron relation for discontinuous phase transitions and the Ehrenfest relation for continuous ones [45,46]. In $Ni_{0.25}Mn_{0.75}TiO_3$, we consider the anomaly at T_N a continuous phase transition, and its size has been determined by means of a same area construction [47]. At $T_N(B = 0$ T) this yields $\Delta\alpha_b = 0.5(1) \times 10^{-6}$ (1/K) and $\Delta\alpha_c = -0.80(15) \times 10^{-6}$ (1/K) (see Figs. 7 and 10 in the SM [37]). Using these values as well as $\Delta c_p = 0.54(11)$ J/(mol K) and the molar volume $V_m = 3.215 \times 10^{-5}$ m^3/mol, the Ehrenfest relation,

$$\left.\frac{\partial T_N}{\partial p_i}\right|_B = T_N V_m \frac{\Delta\alpha_i}{\Delta c_p} \tag{1}$$

yields $\partial T_N/\partial p_b = 1.1(3)$ and $\partial T_N/\partial p_c = -1.7(5)$ K/GPa for uniaxial pressure applied along the b and the c axes, respectively. Furthermore, T_N depicts a small positive hydrostatic pressure dependence of $\partial T_N/\partial p = 0.4(5)$ K/GPa as qualitatively shown by the anomaly in the volume thermal-expansion coefficient at T_N.

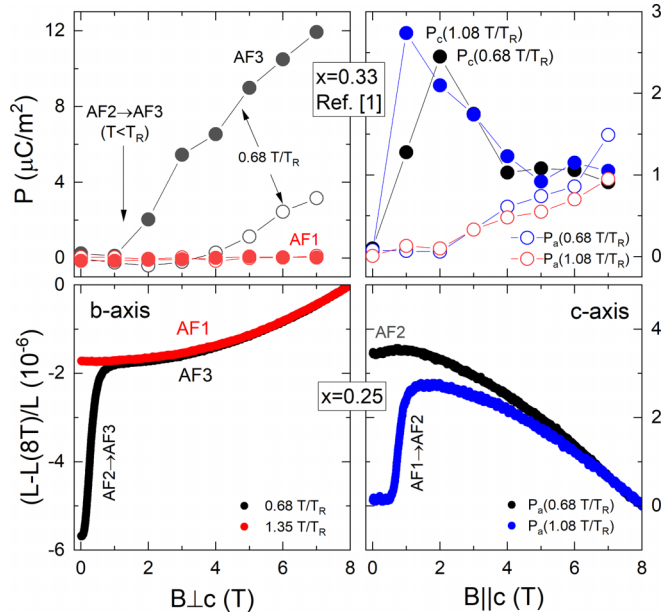

FIG. 12. Magnetic-field dependence of electric polarization ($x = 0.33$, data from Ref. [18] (upper panel; open/filled markers show P_a/P_c) and magnetostriction (lower panel; $x = 0.25$) in $Ni_xMn_{1-x}TiO_3$. In order to compare the results, the data are shown for same values of reduced temperature T/T_R, using $T_R(x = 0.33) = 17.5$ K [18] and $T_R(x = 0.25) = 14.8$ K.

The uniaxial pressure dependencies of T_R are derived from the corresponding jumps $\Delta L_b/L_b = -2.0(2) \times 10^{-6}$, $\Delta L_c/L_c = 3.1(2) \times 10^{-6}$, and $\Delta S = -0.027(3)$ J/(mol K). Using the Clausius-Clapeyron relation for a discontinuous phase transition [45],

$$\left.\frac{\partial T_R}{\partial p_i}\right|_B = V_m \frac{\Delta L_i/L_i}{\Delta S} \tag{2}$$

yields the uniaxial pressure dependencies $\partial T_R/\partial p_b = 2.3(4)$ and $\partial T_R/\partial p_c = -3.7(5)$ K/GPa. Following the phase boundary $T_R(B)$ [AF1 $\rightarrow$ AF2/AF′ in Fig. 9(a)], the signs of the thermal expansion anomalies change at $B \simeq 1$ T implying opposite uniaxial pressure dependencies for AF1 $\rightarrow$ AF2 and AF1 $\rightarrow$ AF3′. The observed changes in pressure dependence and, in particular, the magnetostrictive effects shed light on the recently observed flop of electric polarization from $P \parallel c$ to $P \parallel a$ in $Ni_{0.33}Mn_{0.67}TiO_3$ [18]. Chi *et al.* [18] associate the linear ME response with rotation of the collinear spins away from the c axis for $T < T_R$. Comparison of polarization and magnetostriction data at the same reduced temperatures T/T_R yields the following observations (see Fig. 12): For $B \perp c$, (1) the jump in length at the transition AF2$\rightarrow$ AF3 indicates the onset of finite ME effect. (2) Although magnetostriction is indiscernible in AF3 and AF1, a finite field-induced polarization appears only in AF3, whereas, it is negligible in AF1. (3) For $B \parallel c$, both AF1 and AF2 show the ME effect and P_c peaks at 1 to 2 T. However, whereas, for $T > T_R$ there are anomalies both in P_c and L_c for $T < T_R$, the peak in P_c is not associated

with a jump in $L(B)$. From (1)–(3), we conclude that magnetoelastic coupling is prominent and yields distinct structural anomalies at the phase boundaries as well as differences in the magnetostrictive response of the different magnetic phases and, correspondingly, the different ME regimes. However, observation (2) suggests that the ME effect in $Ni_xMn_{1-x}TiO_3$ may not be directly related to magnetostriction.

V. CONCLUSIONS

To conclude, we report detailed dilatometric, specific heat, and magnetic studies on macroscopic single crystals of $Ni_{0.25}Mn_{0.75}TiO_3$ grown by means of the optical floating-zone method. Our data imply the evolution of long-range magnetic order at $T_N \simeq 35$ K and a spin reorientation at $T_R \simeq 15$ K. The latter is of discontinuous nature and attributed to competing magnetic anisotropies of Mn^{2+} and Ni^{2+} magnetic moments. We find clear anomalies in the length changes at the phase boundaries, indicating pronounced magnetoelastic coupling and sizable pressure dependencies of the associated ordering phenomena, respectively, energy scales. Quantitatively, our analysis yields $\partial T_N/\partial p_b = 1.1(3)$, $\partial T_N/\partial p_c = -1.7(5)$, $\partial T_R/\partial p_b = 2.3(4)$, and $\partial T_R/\partial p_c = -3.7(5)$ K/GPa. Applying magnetic-fields $B \parallel b$ axis yields a sign change in the uniaxial pressure dependence signaling different low-temperature phases. Splitting of the anomalies implies the presence of an intermediate phase AF3′. In addition, our experimental data show short-range magnetic order well above T_N as well as at low-temperatures, weakly coupled moments, and a glass- behavior ($T_{SG} \simeq 3.7$ K). The number of weakly coupled moments is sizable and might be attributed to about 15% of all Mn^{2+} spins present in the material. Glasslike behavior is seen in AC-χ and is further evidenced by quasilinear T dependence of c_p at low temperatures. The observed changes in pressure dependence and, in particular, the magnetostrictive effects shed light on the recently observed flop of electric polarization from $P \parallel c$ to $P \parallel a$ [18], suggesting that the ME effect in $Ni_xMn_{1-x}TiO_3$ appearing at intermediate-doping x does not have a direct magnetostrictive origin.

ACKNOWLEDGMENTS

We are grateful to H. Wadepohl from the Inorganic Chemical Institute of Heidelberg University for performing single-crystal diffraction studies. We acknowledge support by BMBF via the Project SpinFun (Project No. 13XP5088) and by Deutsche Forschungsgemeinschaft (DFG) under Germany's Excellence Strategy EXC2181/1-390900948 (the Heidelberg STRUCTURES Excellence Cluster) and Project No. KL 1824/13-1. L.G. and K.D. acknowledge support by IMPRS-QD. A.E. acknowledges support by DAAD through the GSSP Program. We acknowledge support of the HLD at HZDR, member of the European Magnetic Field Laboratory.

[1] D. Sherrington and S. Kirkpatrick, Phys. Rev. Lett. **35**, 1792 (1975).
[2] M. Kobayashi, K. Katsumata, T. Satō, and Y. Miyako, J. Phys. Soc. Jpn. **46**, 1467 (1979).
[3] S. Murayama, K. Yokosawa, Y. Miyako, and E. F. Wassermann, Phys. Rev. Lett. **57**, 1785 (1986).
[4] G. C. DeFotis, D. S. Mantus, E. M. McGhee, K. R. Echols, and R. S. Wiese, Phys. Rev. B **38**, 11486 (1988).
[5] T. Ono, T. Kato, H. Tanaka, A. Hoser, N. Stüßer, and U. Schotte, Phys. Rev. B **63**, 224425 (2001).
[6] F. Matsubara and S. Inawashiro, J. Phys. Soc. Jpn. **42**, 1529 (1977).
[7] M. Igarashi and K. Nagata, J. Magn. Magn. Mater. **90-91**, 363 (1990).
[8] Y. Ishikawa and S.-i. Akimoto, J. Phys. Soc. Jpn. **13**, 1110 (1958).
[9] L. Bevaart, E. Frikkee, J. Lebesque, and L. De Jongh, Solid State Commun. **25**, 539 (1978).
[10] A. Ito, H. Aruga, E. Torikai, M. Kikuchi, Y. Syono, and H. Takei, Phys. Rev. Lett. **57**, 483 (1986).
[11] A. Ito, H. Aruga, M. Kikuchi, Y. Syono, and H. Takei, Solid State Commun. **66**, 475 (1988).
[12] T. Kurihara, T. Komai, A. Ito, and T. Goto, J. Phys. Soc. Jpn. **60**, 2057 (1991).
[13] A. Ito, H. Kawano, H. Yoshizawa, and K. Motoya, J. Magn. Magn. Mater. **104-107**, 1637 (1992).
[14] H. Yoshizawa, H. Kawano, H. Mori, S. Mitsuda, and A. Ito, Physica B **180-181**, 94 (1992).
[15] Y. Yamaguchi, T. Nakano, Y. Nozue, and T. Kimura, Phys. Rev. Lett. **108**, 057203 (2012).
[16] Y. Yamaguchi and T. Kimura, Nat. Commun. **4**, 2063 (2013).
[17] R. S. Solanki, S.-H. Hsieh, C. H. Du, G. Deng, C. W. Wang, J. S. Gardner, H. Tonomoto, T. Kimura, and W. F. Pong, Phys. Rev. B **95**, 024425 (2017).
[18] S. Chi, F. Ye, H. D. Zhou, E. S. Choi, J. Hwang, H. Cao, and J. A. Fernandez-Baca, Phys. Rev. B **90**, 144429 (2014).
[19] J. B. Goodenough and J. J. Stickler, Phys. Rev. **164**, 768 (1967).
[20] G. Shirane, S. J. Pickart, and Y. Ishikawa, J. Phys. Soc. Jpn. **14**, 1352 (1959).
[21] R. Newnham, J. Fang, and R. Santoro, Acta Crystallogr. **17**, 240 (1964).
[22] H. Kato, Y. Yamaguchi, M. Ohashi, M. Yamada, H. Takei, and S. Funahashi, Solid State Commun. **45**, 669 (1983).
[23] M. Hoffmann, K. Dey, J. Werner, R. Bag, J. Kaiser, H. Wadepohl, Y. Skourski, M. Abdel-Hafiez, S. Singh, and R. Klingeler, Phys. Rev. B **104**, 014429 (2021).
[24] N. Mufti, G. R. Blake, M. Mostovoy, S. Riyadi, A. A. Nugroho, and T. T. M. Palstra, Phys. Rev. B **83**, 104416 (2011).
[25] T. Müller, Order and disorder in the charge and spin structures of YFe2O4-δ and Ni0. 42Mn0. 58TiO3, Ph.D. thesis, RWTH Aachen University, 2018.
[26] K. Dey, S. Sauerland, J. Werner, Y. Skourski, M. Abdel-Hafiez, R. Bag, S. Singh, and R. Klingeler, Phys. Rev. B **101**, 195122 (2020).
[27] K. Dey, S. Sauerland, B. Ouladdiaf, K. Beauvois, H. Wadepohl, and R. Klingeler, Phys. Rev. B **103**, 134438 (2021).

[28] L. Gries, M. Jonak, A. Elghandour, K. Dey, and R. Klingeler, Phys. Rev. B **106**, 174425 (2022).
[29] W. Hergett, C. Neef, H. Wadepohl, H.-P. Meyer, M. M. Abdel-Hafiez, C. Ritter, E. Thauer, and R. Klingeler, J. Cryst. Growth **515**, 37 (2019).
[30] C. Neef, H. Wadepohl, H.-P. Meyer, and R. Klingeler, J. Cryst. Growth **462**, 50 (2017).
[31] K. Dey, Single-crystal growth, magnetic and thermodynamic investigations of ilmenite titanates and lanthanum nickelates, Ph.D. thesis, Heidelberg University, 2021.
[32] J. Rodríguez-Carvajal, Physica B **192**, 55 (1993).
[33] R. D. Shannon, Acta. Crystallogr., Sect. A: Cryst. Phys., Diffr., Theor. Gen. Crystallogr. **32**, 751 (1976).
[34] Y. Skourski, M. D. Kuz'min, K. P. Skokov, A. V. Andreev, and J. Wosnitza, Phys. Rev. B **83**, 214420 (2011).
[35] R. Küchler, A. Wörl, P. Gegenwart, M. Berben, B. Bryant, and S. Wiedmann, Rev. Sci. Instrum. **88**, 083903 (2017).
[36] J. Werner, W. Hergett, M. Gertig, J. Park, C. Koo, and R. Klingeler, Phys. Rev. B **95**, 214414 (2017).
[37] See Supplemental Material at http://link.aps.org/supplemental/10.1103/PhysRevB.108.014406 for additional ac and dc magnetization, specific heat, thermal expansion, and magnetostriction data. It also shows how the anomaly sizes have been determined.
[38] M. E. Fisher, Philos. Mag. **7**, 1731 (1962).
[39] Y. Syono, S.-I. Akimoto, Y. Ishikawa, and Y. Endoh, J. Phys. Chem. Solids **30**, 1665 (1969).
[40] L. J. de Jongh, D. Betts, and D. Austen, Solid State Commun. **15**, 1711 (1974).
[41] Here, we used the Ni content as determined by EDX; using the nominal Ni content does not change the conclusion.
[42] A. Tari, *The Specific Heat of Matter at Low Temperatures* (World Scientific, Singapore, 2003).
[43] W. Fogle, J. Ho, and N. Philipps, J. Phys. Colloq. **39**, C6-901 (1978).
[44] R. Caudron, P. Costa, J. Lasjaunias, and B. Levesque, J. Phys. F: Met. Phys. **11**, 451 (1981).
[45] T. Barron and G. White, in *Heat Capacity and Thermal Expansion at Low Temperatures* (Springer, Berlin, 1999), pp. 153–223.
[46] R. Klingeler, B. Büchner, S.-W. Cheong, and M. Hücker, Phys. Rev. B **72**, 104424 (2005).
[47] R. Küchler, Thermische Ausdehnung und divergierendes Grüneisenverhältnis in Schwere-Fermionen-Systemen, Dissertation, Technische Universität Dresden, Dresden, 2005.